

1 **Methodology to determine the coupling of continental clouds with surface and**
2 **boundary layer height under cloudy conditions from lidar and meteorological**
3 **data**

4

5 Tianning Su¹, Youtong Zheng², and Zhanqing Li¹

6

7 ¹Department of Atmospheric and Oceanic Sciences & ESSIC, University of Maryland
8 , College Park, Maryland 20740, USA

9 ²The Program in Atmospheric and Oceanic Sciences, Princeton University, and
10 NOAA/Geophysical Fluid Dynamics Laboratory, Princeton, NJ, USA

11

12

13

14

15

16

17

18 *Correspondence to:* zhanqing@umd.edu; tianning@umd.edu

19 **Abstract.**

Formatted: Font: Bold

20 The states of coupling between clouds and surface or boundary-layer have been
21 investigated much more extensively for marine stratocumulus clouds than for
22 continental low clouds, partly due to more complex thermodynamic structures over land.
23 A manifestation is a lack of robust remote sensing methods to identify coupled and
24 decoupled clouds over land. ~~Here~~ Following the idea for determining cloud coupling
25 over the ocean, we have generalized the concept of coupling and decoupling to low
26 clouds over land, based on potential temperature profiles. Furthermore, by using ample
27 measurements from ~~a~~ lidar and a suite of surface meteorological instruments at the U.S.
28 Department of Energy's Atmospheric Radiation Measurement Program's Southern
29 Great Plains site from 1998 to 2019, we have developed a method to simultaneously
30 retrieve the planetary boundary layer (PBL) height (PBLH) and coupled states under
31 cloudy conditions during the daytime. The new lidar-based method jointly uses the
32 differences between ~~relies on heights of the PBLH, the lifted condensation level, and the~~
33 cloud base position to diagnose the cloud coupling. ~~As a result, T~~ The coupled states
34 derived from this lidar-based method ~~lidar show strong~~ are highly consistently with
35 those derived from radiosondes. Retrieving the PBLH under cloudy conditions that has
36 been a persistent problem in lidar remote sensing, is resolved in this study. Our method
37 can lead to high-quality retrievals of the PBLH under cloudy conditions, and the
38 determination of cloud coupling states. With the new method, we find that coupled
39 clouds are sensitive to changes in the PBL, with a strong diurnal cycle, whereas
40 decoupled clouds and the PBL are weakly related. Since coupled and decoupled clouds

41 have distinct features, our new method offers an advanced tool to separately investigate
42 them in climate systems.

43 1 Introduction

44 A large fraction of low clouds is driven by surface fluxes through the conduits of
45 the planetary boundary layer (PBL) over land (e.g., Betts, 2009; Ek and Holtslag, 2004;
46 Golaz et al., 2002; Teixeira and Hogan, 2002; Zheng et al., 2020; Wei et al., 2020;
47 Santanello et al., 2018). This is a coupled cloud-surface system (Cheruy et al., 2014;
48 Zheng and Rosenfeld, 2015; Wu et al., 1998). However, not all low clouds respond to
49 surface forcing. Those clouds without close interactions with the local surface are
50 considered to be in a decoupled state. Given that the PBL is, by definition, the lowest
51 atmospheric layer influenced by the underlying surface (Stull, 1988), to what degree
52 the PBL top overlaps with cloud bases becomes a good criterion to separate coupled
53 and decoupled low clouds.

54 Conventionally, the “coupled state” of a cloud-topped marine boundary layer
55 implies that the moist conserved variables are vertically well mixed within the PBL
56 (Bretherton and Wyant, 1997; Dong et al., 2015; Zheng and Li, 2019; Zheng et al.,
57 2018). However, such a definition cannot be simply applied to clouds over land since
58 ~~the moist conserved variables typically show considerable variations due to the~~
59 ~~relatively complex thermodynamics (Driedonks, 1982; Stull, 1988).~~ The definition and
60 the determination methods of the PBL over land ~~also widely~~ differ from those over
61 ocean (Garratt, 1994; Vogelezang and Holtslag, 1996). The concept of coupled and
62 decoupled states is typically used to characterize marine stratocumulus clouds due to
63 their large-scale coverages (Nicholls, 1984). Since stratocumulus only constitutes a
64 relatively small portion of continental clouds (Warren et al., 1986), we attempt to extend

65 the concept of coupling and decoupling to characterize low clouds over land. Due to
66 the relatively complex thermodynamics, the moisture conserved variables (e.g., total
67 water mixing ratio and liquid potential temperature) may not be a near-constant in the
68 coupled sub-cloud layer (Driedonks, 1982; Stull, 1988).

69

70 Following parcel theory, the lifted condensation level (LCL) has been used to
71 diagnose a coupled cloud, based on the distance between the LCL and the cloud base
72 (e.g., Dong et al., 2015; Glenn et al., 2020; Zheng and Rosenfeld, 2015; Zheng et al.,
73 2020). When potential temperature and humidity are uniformly distributed in the
74 vertical, the LCL should be consistent with the cloud base for coupled cases. However,
75 the cloud base for coupled cases can considerably differ from the LCL over land
76 because potential temperature and humidity have large variabilities in the vertical scale
77 within the PBL over land (Driedonks, 1982; Guo et al., 2016; Stull, 1988; Su et al.,
78 2017a). To address the limitation in the LCL method, we attempt to develop a remote
79 sensing method to distinguish coupled and decoupled clouds over land.

80 Since the PBL height (PBLH) is the maximum height directly influenced by surface
81 fluxes, we consider coupling with the PBL equivalent to coupling with the land surface.
82 Thus, we use the PBLH as a critical parameter to diagnose the coupling between clouds
83 and the land surface. The degree of coupling may thus be gauged in terms of
84 quantitative differences between the cloud base and the PBL top. Such differences can
85 be determined in a height coordinate system or in a potential temperature coordinate
86 system (Kasahara, 1974). For this purpose, ground-based lidar has great potential

87 because it can continuously track the development of the PBL (Demoz et al., 2006;
88 Hageli et al., 2000; Sawyer and Li, 2013; Su et al., 2017b) and clouds (Clothiaux et al.,
89 2000; Platt et al., 1994; Zhao et al., 2014) at high temporal and vertical resolutions.

90 By jointly using lidar measurements and meteorological data from the U.S.
91 Department of Energy's Atmospheric Radiation Measurement (ARM) Southern Great
92 Plains (SGP) site (36.6°N, 97.48°W), we attempt to identify coupled and decoupled low
93 clouds during the daytime. Unlike previous studies that use the LCL or radiosonde (RS)
94 data to diagnose coupled clouds (e.g., Dong et al., 2015; Zheng and Rosenfeld, 2015),
95 this study developed a lidar-based method to determine the status of cloud coupling
96 over land at a high temporal resolution.

97 The paper is organized as follows. Section 2 describes the measurements and data.
98 Section 3 describes the new methodology in terms of the definition and implementation.
99 The performance of the method is demonstrated in Section 4, and a summary is
100 presented in Section 5.

101

102 **2 Data Descriptions**

103 *2.1 Radiosonde*

104 RS launches took place at least four times per day at the ARM SGP site, usually at
105 0030, 0630, 1230, and 1830 local time (LT). Holdridge et al. (2011) provide technical
106 details about the ARM RS (<https://www.arm.gov/capabilities/instruments/sonde>). In
107 this study, we consistently use daylight saving time (Coordinated Universal Time -5 h)

108 as local time throughout the year to avoid inconsistencies between summer and winter.
109 Besides the routine measurements, there are fewer, but still considerable numbers of
110 RS data obtained at other times of the day (e.g., 0930, 1200, 1300, 1530, and 1900 LT).
111 These supplemental RS samples at other times comprise ~10% of the total number of
112 cases. RS data from 0630–1900 LT are utilized in this study. The vertical resolution of
113 RS data varies according to the rising rate of the balloon, but measurements are
114 generally taken ~10 m apart. We further vertically average the RS data to achieve a
115 vertical resolution of 5 hPa.

116 There are several methods to determine PBLH from RS-measured temperature,
117 pressure, and humidity profiles. They include, among others, the parcel method
118 (Holzworth, 1964), the gradient methods (Stull, 1988; Seidel et al., 2010), and the
119 Richardson number method (Vogelezang and Holtslag, 1996). After examining the
120 previous methods, Liu and Liang (2010) proposed a different approach to determine the
121 PBLH that is valid under different thermodynamic conditions. The robust performance
122 was demonstrated over the SGP site and in other major field campaign sites around the
123 world (Liu and Liang, 2010). Thus, we adopted this method to calculate PBLH from
124 RS data in this study. The potential temperature is corrected as the virtual potential
125 temperature, θ_v , using the water vapor mixing ratio [WVMR; $\theta_v = (1 + 0.61\text{WVMR})$].
126 The virtual potential temperature does not include a correction for the liquid water
127 content profile, as this is challenging to measure in many conditions. Therefore, the
128 virtual potential temperature is not conserved during moist convection. Since we mainly
129 focus on the sub-cloud atmosphere, this is not a serious problem. Moreover, we use

130 scaled RS moisture profiles normalized by the total precipitable water vapor derived
131 from the microwave radiometer (<https://www.arm.gov/capabilities/vaps/lsonde>,
132 Revercomb et al., 2003).

133

134 *2.2 Micropulse lidar (MPL) system*

135 MPL backscatter profiles were collected at the SGP site from September 1998 to
136 July 2019 with high continuity (Campbell et al., 2002). Technical details and data
137 availability can be found at the website
138 <https://www.arm.gov/capabilities/instruments/mpl>. The backscatter profiles have a
139 vertical resolution of 30 m. MPL signals have an initial temporal resolution of 10–30 s
140 and are averaged every 10 min for this study. Due to the inherent problem of lidar
141 observations, there is a ~0.2-km near-surface “blind zone”. Following the standard
142 lidar-data processing, background subtraction, signal saturation and overlapping, after-
143 pulse and range corrections are applied to the raw MPL data (Campbell et al., 2002,
144 2003). Questionable data are excluded based on the quality-control flags.

145

146 *2.3 Cloud product*

147 The MPL can be used to detect cloud layers based on signal gradients (Platt et al.,
148 1994). Lidar-based methods are accurate for determining the cloud-base height (CBH)
149 but may miss information about the cloud top due to the signal saturation within an
150 optically thick cloud (Clothiaux et al., 2000). Under this condition, the cloud radar

151 provides a better estimation of the cloud-top height (CTH). In this study, we directly
152 use an existing quality-controlled cloud product, CLDTYPE/ARSCL
153 (<https://www.arm.gov/capabilities/vaps/cldtype>), which combines information from
154 the MPL, ceilometer, and cloud radar to determine the vertical boundaries of clouds
155 (Clothiaux et al., 2000; Flynn et al., 2017). For the lowest cloud base, the best
156 estimation from laser-based techniques (i.e., MPL and ceilometer) is used. The original
157 temporal resolution of the CLDTYPE/ARSCL product is 1 min, averaged to a 10-min
158 temporal resolution. To avoid averaging jumps in signal between different clouds, a
159 cloud is considered to be continuous if its base height varies less than 0.25 km between
160 two consecutive profiles.

161

162 **3 Methodology**

163 *3.1 Definition of coupled and decoupled clouds based on thermodynamics*

164 The definition of the state of cloud-surface coupling over land is a critical question.
165 For marine stratocumulus, coupled clouds are identified when the liquid water potential
166 temperature varies less than a certain threshold (i.e., 0.5 K) below the cloud base (Jones
167 et al., 2011). We try to extend the concept of coupling and decoupling to clouds over
168 land. The PBL over land is typically buoyancy driven and controlled by surface fluxes
169 during the daytime. We consider a cloud is in the coupled state when it strongly interacts
170 with the buoyancy fluxes within the PBL.

171 Figure 1 presents the idealized vertical profiles of virtual potential temperature (θ_v)
172 under the clear-sky, coupled cloud, and decoupled cloud. A superadiabatic surface layer
173 exchanges the heat fluxes between the surface and PBL. The outer layer and
174 entrainment zone are turbulently coupled with the surface, and thus, are considered as
175 the coupled regime. Meanwhile, the free atmosphere is considered as the decoupled
176 regime. Theoretically, θ_v is constant in the outer layer, and follows the wet adiabatic
177 lapse rate in the cloud layer. Although the profiles of θ_v in the real atmosphere can
178 largely differ from the idealized profiles, the relative position between the cloud layer
179 and capping inversion of entrainment zone is clear. For the coupled cases, the cloud
180 base is below the capping inversion of entrainment zone. For the decoupled cases, the
181 cloud base is above the capping inversion. ~~Based on this feature, we can use the profiles~~
182 ~~of virtual potential temperature (θ_v) profiles in the sub-cloud layer to determine the~~
183 ~~coupling state of continental clouds. It should be noted that the virtual potential~~
184 ~~temperature is not conserved in a moist adiabatic process and thus would decrease~~
185 ~~within a cloud layer. On the other hand, the liquid potential temperature would remains~~
186 ~~a near-constant within the stratocumulus. Since we use the profiles of potential~~
187 ~~temperature profiles in the sub-cloud layer to diagnose the cloud coupling, there will~~
188 ~~be no difference in the identification results by using the virtual potential temperature.~~
189 Following the previous studies (Jones et al., 2011; Dong et al., 2015), we attempt
190 to use the variations in the potential temperature within the sub-cloud layer to diagnose
191 the cloud coupling. For determining a suitable threshold,

- Formatted: Font: Not Bold
- Formatted: Font: Not Bold
- Formatted: Font: Not Bold
- Formatted: Font: Not Bold
- Formatted: Font: Not Bold
- Formatted: Font: Not Bold
- Formatted: Font: Not Bold
- Formatted: Normal, Left, Don't adjust right indent when grid is defined, Space Before: 0 pt, Don't adjust space between Latin and Asian text, Don't adjust space between Asian text and numbers, Pattern: Clear

192 ~~w~~We first look at several examples of profiles of θ_v and WVMR from the RS
193 (Figure 2). If the CBH is lower than the PBLH, the cloud is affected by turbulence and
194 buoyancy fluxes in the PBL, such as the cases shown in Figure 2a. Note that the PBLH
195 is not an absolute boundary limiting turbulence and buoyancy fluxes. Due to the
196 overshooting of rising air parcels, we use a range to screen the condition of coupled
197 clouds. As shown in Figure 2b, even when the CBH is slightly above the PBLH,
198 WVMR and θ_v are still relatively consistent between the cloud layer and the PBL and
199 show large step signals at the cloud top. ▲

200 Figure 2c-d shows a clear inversion layer between the cloud base and the PBL top,
201 and the difference in θ_v between the CBH and the PBLH ($\Delta\theta_v$) is relatively large.
202 Such a notable inversion layer prevents the buoyancy fluxes within the PBL from
203 reaching the cloud base, leading to the decoupling between the cloud and the PBL.

204 ~~Overall, we consider using $\Delta\theta_v$ as the key factor to determine cloud coupling. Overall,~~
205 ~~whether there is a clear inversion between the cloud base and the PBL top is the key~~
206 ~~factor in determining coupling and decoupling. In this aspect, $\Delta\theta_v$ is the key factor. In~~

207 Figure 2, $\Delta\theta_v$ for coupled cases (a-c) is -0.32 K and 0.31 K, respectively, and $\Delta\theta_v$
208 for decoupled cases (d-e) is 1.47 K and 5.0 K, respectively.

209 Therefore, instead of giving a height range to limit the differences between CBH
210 and PBLH, we consider using the differences in θ_v between CBH and PBLH to
211 determine the threshold for distinguishing coupled and decoupled clouds. For
212 convenience, we use $\Delta\theta_v$ to refer to the difference in θ_v between the CBH and the
213 PBLH ($\Delta\theta_v = \theta_v^{\text{CBH}} - \theta_v^{\text{PBLH}}$). For decoupled cases, the cloud base is above the

Formatted: Font: Times New Roman, 12 pt, Font color:

Formatted: Font: 12 pt, Font color: Black

Formatted: Font: 12 pt, Font color: Black

Formatted: Font: Times New Roman, 12 pt, Font color:

Formatted: Font: 12 pt, Font color: Black

Formatted: Font: 12 pt, Font color: Black

Formatted: Font: Times New Roman, 12 pt, Font color:

Formatted: Font: Times New Roman, 12 pt, Font color:

214 capping inversion of entrainment zone. There is a notable inversion in θ_v between
215 PBL top and decoupled cloud base. Thus, we identify the cases satisfying $\Delta\theta_v > \delta_s$ as
216 being in a decoupled state. Correspondingly, we identify the cases satisfying $\Delta\theta_v < \delta_s$
217 as being in a coupled state. We set the range of CBH to between 0 and 4 km and
218 excluded cases of deep convection (i.e., $CBH < 4$ km and $CTH > 6.5$ km). In the
219 previous studies for marine clouds, the difference in the potential temperature between
220 the CBH and the near-surface is used as the criterion (Jones et al., 2011; Dong et al.,
221 2015). However, we use the potential temperature at the PBL top instead of the potential
222 temperature near the surface. This change is due to the relatively complex
223 thermodynamics structure over the land. The large variation in the potential temperature
224 within the surface layer would notably affect the result. Hence, we use the potential
225 temperature ~~over~~above the PBL top to replace those values near the surface.

226 As the basic framework of PBL, the slab model assumes that θ_v is constant within
227 the PBL (Wallace and Hobbs, 2006). Under this assumption, δ_s can be set as 0.
228 However, there are certain variations in θ_v within the PBL, which can cause inversions
229 with relatively small magnitudes between the cloud base and PBL top. Figure 3a
230 presents the inversion strength in θ_v within PBL during the daytime. Specifically,
231 inversions represent the layers with continuously increased structures of θ_v . For an
232 inversion layer, the inversion strength is calculated as the differences in θ_v between the
233 top and bottom of the layer. The inversions near surface or across the PBL top are
234 excluded. Besides the capping inversion and surface inversion, the inversion strength
235 within PBL is typically below 1K. Therefore, we set δ_s as 1 K, which is the same as

236 the criterion for determining stable or convective conditions (Liu and Liang, 2010).
237 Furthermore, we demonstrate the probability density function (PDF) of $\Delta\theta_v$ for the
238 low cloud cases. Coupled and decoupled clouds are classified by the threshold of δ_s
239 (1 K). Through the development of PBL, boundary layer clouds frequently occur in the
240 entrainment zone, and form a coupled cloud-PBL system. For such coupled systems,
241 θ_v at cloud top and PBL top is highly consistent for the majority of cases. Thus, the
242 PDF of $\Delta\theta_v$ shows significantly high values for the range of -2 K to 0.5 K in the
243 coupled regime. Meanwhile, the PDF of $\Delta\theta_v$ is evenly distributed in the decoupled
244 regime. Since we only analyze low clouds, the PDF of $\Delta\theta_v$ slowly decrease when $\Delta\theta_v$
245 is above 10 K.

246 Based on the variations in θ_v within PBL, we set δ_s as 1 K. However, it should
247 note that it is not an absolute value. A similar threshold of 0.5 K has been used for
248 marine stratocumulus (Jones et al., 2011; Dong et al., 2015). Comparing to the marine
249 condition, θ_v show greater variabilities over land. Hence, the threshold is
250 correspondingly larger. On the other hand, since the threshold of 1 K is in the low PDF
251 regime (Figure 3b), the small changes in this value would not notably affect the
252 identifications. Specifically, a 0.1 K difference in δ_s will lead to a 0.5% difference in
253 the identification of coupled cloud.

254 Same to the previous studies (Jones et al., 2010; Dong et al., 2015; Zheng and
255 Rosenfeld, 2015), we identified the coupled clouds as the thermodynamics coupling
256 between surface and cloud base. However, it is an open question whether the entire
257 cloud layer is coupled for coupled cases. It depends on whether the liquid water

258 potential temperature is conserved within the cloud layer, which represents a moisture
259 adiabatic process. This issue is closely related to the cloud types. In the cloud
260 parameterizations, the entire stratocumulus layer is considered to be well-mixed,
261 while the cumulus-capped layer is usually partially mixed (Lock, 2000). For
262 stratocumulus clouds, the entire cloud layer and PBL are typically fully coupled with
263 surface, when the cloud base is coupled with surface. For the cumulus-capped PBL, the
264 entire cloud layer may not be completely coupled, despite the coupling between cloud
265 base and surface. The well-established parameterizations are supported by many
266 observational studies (e.g., Betts, 1986; Storer et al., 2015; Berkes et al., 2016, de Roode
267 and Wang, 2006; Ott et al., 2009).

268

269 *3.2 Lidar-based method to identify coupled and decoupled clouds*

270 *3.2.1 Method description*

271 Given the rapid change in clouds over land, RS observations have limitations when
272 it comes to tracking cloud development due to the coarse temporal resolution and
273 drifting of the balloon. We thus further developed a lidar-based method to identify the
274 coupled states of clouds based on our new algorithm for retrieving the PBLH that can
275 better track the diurnal variations in PBLH than conventional lidar-based approaches
276 (Su et al., 2020). We adapted this algorithm for retrieving the PBLH and developed a
277 new scheme to deal with cloudy conditions. Following the original method (Su et al.
278 2020), the rainy cases are eliminated in the quality control process. The principles
279 behind the PBLH algorithm are stated next for completeness.

280 Our new PBLH algorithm can retrieve the PBL variability from the MPL under
281 Different Thermo-Dynamic Stability (thus named the DTDS algorithm) conditions,
282 taking into account the vertical coherence and temporal continuity of the PBLH. First,
283 we identify the local maximum positions (LMPs; range: 0.25–4 km) in profiles of the
284 wavelet covariance transform function derived from lidar backscatter (Brooks, 2003).
285 These LMPs are the potential positions of the PBLH. We can use the PBLH derived
286 from morning RS soundings as the starting point. Without morning RS soundings, the
287 algorithm can still work well, with the lowest LMPs selected as the starting point, which
288 reduces by 0.02–0.05 the correlation coefficient between MPL-derived and RS-derived
289 PBLHs (Su et al., 2020).

290 To ensure good continuity, we select the closest LMP to the earlier position of the
291 PBLH. Different stages of PBL development are considered. DTDS-derived PBLHs
292 likely increase during the growth stage and decrease during the decaying stage, but the
293 algorithm is also able to identify decreases during the growth stage or increases during
294 the decaying stage based on the selection scheme described by Su et al. (2020). There
295 are multiple step signals in the backscatter profiles when complex aerosol structures
296 (e.g., the residual layer) are present, leading to multiple LMPs. Based on temporal
297 continuity, we select the appropriate LMP as the position of the PBL top. However,
298 PBLH retrievals still suffer from relatively low accuracies under stable conditions
299 because of the weak vertical mixing and residual layer.

300 Clouds induce strong step signals in the lidar backscatter, further considerably
301 affecting PBLH retrievals. Su et al. (2020) only considered cases where the low cloud

302 top coincided with the previous PBL top, excluding other low-cloud cases (> 60% of
303 all low-cloud cases). Here, we specifically consider coupled and decoupled states of
304 low clouds. Due to the MPL's ~0.2-km blind zone, we only analyze the PBLH and CBH
305 above 0.2 km. Figure 4 presents the flow chart describing the updated DTDS algorithm.
306 In particular, we jointly use PBL development and the LCL to diagnose the states of
307 coupling or decoupling. In ideal situations, LCL, PBLH, and CBH are highly consistent
308 with each other for coupled clouds. But for real conditions, we only require that either
309 the LCL or the PBLH coincides with the CBH for identifying coupled cases, with
310 another parameter serving as an additional constraint. Specifically, a coupled cloud
311 needs to occur within a certain range of LCL and the previous position of the PBL top.

312 For the DTDS algorithm, five empirical parameters are used, including A_1 , A_2 ,
313 A_3 , A_4 , A_5 . As listed in the Table 1, $A_1 - A_5$ are set as 0.7, 0.2, 0.15, 1.35, and 1.1,
314 respectively. A cloud at time i is identified as being in the coupled state if the CBH is
315 less than $[H(i - 1) + 0.2 \text{ km } (A_2)]$ and $[\text{LCL} + 0.7 \text{ km } (A_1)]$. This step moves 39.5%
316 of low cloud cases to the category of decoupled clouds. A cloud is also considered to
317 be in a coupled state if the CBH is coincident with the LCL within 0.15 km (A_3), and
318 the CBH is less than $[H(i - 1) + 0.7 \text{ km } (A_1)]$, where $H(i - 1)$ represents the
319 PBLH at time $(i - 1)$. This step further moves 17.8% of the remaining cases to the
320 category of decoupled clouds.

321 The LCL is calculated from surface meteorological data (relative humidity,
322 temperature, pressure) at the SGP site based on an exact expression (Romps, 2017).
323 Specifically, Romps. (2017) proposed an exact, explicit, analytic expression for LCL as

324 a function of surface meteorology. Compared to the previous approximate expressions,
325 some of which may have an uncertainty in the order of hundreds of meters, the Romps
326 expression can be considered as the precise value. The uncertainty of empirical vapor
327 pressure data may lead to a bias of ~5-m (Romps, 2017), which may be neglected in the
328 analyses.

329 After determining the coupling or decoupling state of a cloud, we retrieve $H(i)$
330 (i.e., PBLH at time i) based on the cloud state. For decoupled cases, we use the same
331 strategy for a clear sky to retrieve the PBLH. Based on the selection scheme in the
332 DTDS algorithm, the LMP below the CBH is selected as $H(i)$. For coupled cases, we
333 jointly use CBH and CTH to determine PBLH. During the warm season, active cumulus
334 often occurs in the upper part of the PBL with strong surface heating, so the CBH can
335 be generally regarded as the PBLH (Stull, 1988; Wallace and Hobbs, 2006). Under this
336 condition, the CBH coincides with the previous PBL top. Therefore, if $[CTH \geq$
337 $PBLH_{30min} + 0.2 km (A_2)]$, we set $H(i) = A_5 CBH$, where $PBLH_{30min}$ is the
338 average value of the PBLH within 30 min of the prior time i . Hence, A_5 would be a
339 critical parameter for the PBLH estimation. On the other hand, if $[CTH <$
340 $PBLH_{30min} + 0.2 km (A_2)]$, we set $H(i)$ equal to the minimum between CTH and the
341 product $A_4 * CBH$. This step is designed for thin clouds or some stratiform clouds. In
342 particular, $A_5 * CBH$ can be notably larger than the CTH for a thin cloud. Under this
343 situation, we tend to use CTH to denote the PBL top. This step has little impact on the
344 detection of surface-cloud coupling, but can assure that the CTH of the coupled cloud
345 is always higher than the retrieved PBLH to fit the real situation.

346 After retrieving $H(i)$, we consider that the cloud above the PBLH is still coupled
347 if $[CBH < H(i) + 0.2 \text{ km } (A_2)]$. Moreover, we added an upper limit for all PBLH
348 retrievals. If $[H(i) > LCL + 0.7 \text{ km } (A_1)]$, we adjust $H(i)$ as the maximum LMP
349 below the LCL. The new DTDS method combines lidar measurements and surface
350 meteorological observations and can simultaneously retrieve the PBLH and cloud states.

351

352 *3.2.2 Selection of empirical parameters*

353 The states of coupling and decoupling are diagnostic parameters rather than explicit
354 expressions. Similar to the other methods for retrieving PBLH (e.g., Brooks, 2003; Liu
355 and Liang, 2010), multiple empirical parameters are used to determine PBLH. As listed
356 in Table 1 lists, we discussed the selection of five empirical parameters in the algorithm.
357 These parameters are related with three factors, including LCL, PBLH, CBH. The
358 sensitivity to the selection of these parameters is presented. The detailed impacts of
359 variations in these parameters on the retrievals of cloud coupling and PBLH will be
360 discussed in this section.

361 Note that we used the CTH and $A_4 * CBH$ as the upper limits for PBLH retrievals in
362 the DTDS algorithm. For coupled cases, these two limits are generally close to or above
363 the position of the PBL top. Only 2% (3%) of total cases meet the condition that the
364 RS-derived PBLH is 0.25 km higher than the CTH ($A_4 * CBH$). Section 4 presents the
365 detailed relationships between CBH, CTH, and PBLH. In the DTDS method, CTH
366 serves as the upper limit for PBLH under the condition of coupled shallow cumulus.

367 Similar to previous studies, we can also use the LCL as the standard to identify
368 coupled clouds (Dong et al., 2015; Zheng and Rosenfeld, 2015). We assume a cloud is
369 coupled if $|\text{CBH} - \text{LCL}| < \Delta h$. By using ~ 7500 RS profiles, the cloud coupling state
370 derived from the virtual potential temperature method (Section 3.1) is considered as the
371 ground truth for evaluation. Figure 5a shows the commission errors and omission errors
372 for different criteria. Here, the commission error is calculated as the percentage of
373 decoupled clouds misidentified as coupled clouds. The commission error can also be
374 called a “false positive”, as the former is a common term for describing the nature of
375 an error in identification. The omission error is calculated as the percentage of coupled
376 clouds that have not been identified under this criterion. By using the LCL, we can
377 obtain a relatively low commission error if the criterion is less than 0.15 km and a
378 relatively low omission error if the criterion is greater than 0.7 km. Thus, we set A_1
379 and A_3 as 0.7 and 0.15 in the DTDS method to exclude and to select cases of coupled
380 clouds. We can also use the RS-derived PBLH as the criterion (Figure 5b).

381 Despite the coarse temporal resolution, the RS-derived PBLH can be a good
382 criterion to use to distinguish between coupling and decoupling. If we consider a
383 coupled cloud as a cloud where $(\text{CBH} < \text{RS-derived PBLH} + 0.2 \text{ km})$, both commission
384 and omission errors are $\sim 5\%$. Therefore, we primarily use $[\text{PBLH} + 0.2 \text{ km} (A_2)]$ in the
385 DTDS method to identify coupled and decoupled regimes. As cloud can considerably
386 affect with lidar backscattering and generate large signal variations, we jointly use lidar
387 backscattering, the previous position of PBL top, and LCL to determine the surface-
388 cloud coupling and PBLH. In particular, the LCL constraint in the algorithm notably

389 reduces the absolute biases in PBLH retrievals under cloudy conditions by 9.3%.

390 Moreover, we test the sensitivity of selecting these empirical parameters. Figure 6
391 presents the commission errors and omission errors in the identifications of coupled
392 clouds for selecting different values of empirical parameters. Among these parameters,
393 A_2 is the critical one, which would notably affect the identification results. In general,
394 A_2 determine the maximum differences between PBLH and CBH for coupled cases. If
395 $[CBH-PBLH > A_2]$, we consider the cloud is under the decoupled state. Thus, the
396 identification method is quite sensitive to A_2 . Selecting a low value of A_2 would
397 neglect many coupled cases, which leads to a high omission error. Meanwhile, selecting
398 a high value of A_2 would misclassify many coupled cases, which leads to a high
399 commission error. After a trail and error, A_2 is set as 0.2 km to balance the omission
400 and commission errors. The selections for other parameters are not sensitive for the
401 coupled cloud identifications. We can choose them from a reasonable range.

402 As a by-product of this method, we also pay attentions to the PBLH retrievals under
403 cloudy conditions. Figure 7 presents the mean absolute biases and correlation
404 coefficients between PBLH derived from lidar and radiosonde for selecting different
405 values of empirical parameters. To match the scope of this study, we only analyze the
406 low cloud conditions. For retrieving PBLH under cloudy conditions, A_2 is the critical
407 parameter. The variations in correlation coefficients under different values of empirical
408 parameters are small with a range of 0.81-0.82. However, the absolute biases can
409 considerably differ under different values of A_5 . In general, A_5 represents the ratio
410 between CBH and PBLH under coupled conditions. If A_5 is above 1.1, PBLH

411 retrievals under cloudy conditions are overestimated. We set A_5 as 1.1 to achieve a
412 relatively low bias and a relatively high correlation coefficient at the same time. For
413 other parameters, the selections from reasonable ranges would not notably affect the
414 PBLH retrievals.

415 In short, selections of these empirical parameters are based on the overall
416 relationship between cloud and PBL under the coupled and decoupled states. In our
417 method, the selection of A_2 is critical for the identifications of coupled clouds, while
418 the selection of A_5 is critical for the PBLH retrievals under cloudy conditions. The
419 selections of other parameters are not sensitive.

420

421 **4 Results**

422 Figure 8 illustrates four examples of PBLH retrievals and cloud states derived from
423 the DTDS algorithm for 27 October 2011, 31 July 2002, 19 March 2000, and 1 May
424 2012. Figure 8a depicts coupled shallow cumulus occurring at noontime at the PBL top.
425 With a weak surface flux of $\sim 200 \text{ W m}^{-2}$, this shallow cumulus cloud appeared for less
426 than an hour. Figure 8b shows a developed coupled cumulus cloud. With a strong
427 surface flux of $\sim 500 \text{ W m}^{-2}$, this coupled cloud continuously developed during the
428 daytime. Figure 8c presents the case of a daylong coupled cloud. After the passage of a
429 frontal system that day, stratocumulus occurred during the morning with a cloud
430 thickness of 0.5 km. Through the development of the PBL, the thick stratocumulus
431 cloud was broken up by the strong turbulences, transforming into shallow cumulus
432 clouds. Figure 8d shows the case of an active coupled cloud, which is generally

433 associated with a large amount of convective available potential energy. Even though
434 coupled clouds can differ in appearance and variability throughout the day, the common
435 feature is the coherent variation between the cloud base and the PBL top. The LCL is a
436 relevant parameter and can differ from the PBLH and the CBH for some coupled cases
437 (e.g., Figure 8b-c).

438 The identification accuracy, or disparity between different methods, are evaluated
439 in terms of the selected criteria, for which the identification method based on $\Delta\theta_v$ is
440 regarded as the “truth”, as described in Section 3.1. Hereafter, all results are analyzed
441 for the period of 1000–1900 LT, so early-morning data are not used. The commission
442 error is 10.1%, and the omission error is 6.8% for the DTDS method. Note that lidar-
443 based PBLH methods generally suffer from relatively low accuracy under stable
444 atmospheric conditions. Following Liu and Liang (2010), we identified stable PBLs
445 from RS measurements. Since coupled clouds are driven by relatively strong buoyancy
446 fluxes, only 1% of total cases of coupled clouds occurred under stable PBL conditions
447 during the study period (0700–1900 LT). Therefore, the relatively low accuracy for
448 stable PBLs is not a major problem in this study.

449 Figure 5 also compares the accuracy between the DTDS and LCL methods. Based
450 on the LCL alone, we cannot choose an appropriate criterion to achieve a lower
451 commission error and omission error simultaneously. Thus, we do not use the LCL as
452 the single standard to detect the coupling and decoupling of low clouds in our study. As
453 diagnostic parameters, different methods inevitably produce different results regarding
454 coupling and decoupling. Although we consider the method based on $\Delta\theta_v$ as the

455 standard, it still suffers from uncertainties arising from balloon drifting. From this
456 perspective, it is hard to conclude which method is the best. Since it determines the
457 PBLH based on aerosol backscattering, the lidar-based method may be more
458 representative of the coupling between a cloud and the aerosol layer near the surface
459 when clear skies occur, at least during a short window of time.

460 Figure 9a-b presents the occurrence frequencies of the CBH and the CTH at
461 different heights. Despite the same variation ranges, clouds are mostly coupled if the
462 CBH is lower than 1 km, while decoupled clouds dominate if the CBH is higher than 3
463 km. Figure 9c-d shows the changes in the coupled fraction (ratio of coupled cases to
464 total cases) with different CBHs and CTHs. The coupled fraction is about 90% if the
465 CBH is lower than 1 km and decreases to 2% for CBHs above 3 km. Although the CBHs
466 for coupled cases are generally less than 3 km, CTHs for coupled cases can be much
467 higher. Coupled clouds still account for around 10% of the cases with CTHs above 6
468 km.

469 Figure 10 shows scatter plots between CBH, CTH, PBLH, and LCL for coupled
470 and decoupled clouds. For coupled clouds, there is a generally strong correlation
471 between CBH, LCL, and PBLH, contrary to the weak relationships of decoupled cases.
472 The relationship between CTH and RS-derived PBLH is complicated. For shallow
473 cumulus clouds, their tops can be considered as PBL tops for the coupled state, while
474 the cloud top is considerably above the position of the PBL top for active cumulus
475 clouds. We also note that the accuracy of CTH retrievals is generally lower than the
476 accuracy of CBH retrievals (Clothiaux et al., 2000). As CTH is not a criterion for cloud

477 coupling, the accuracy of CTH would not affect the identification of coupled cloud, but
478 may affect the PBLH retrievals for the coupled cloud cases. Meanwhile, despite the
479 laser-based detection of CBH is considered as the standard method (Platt et al., 1994;
480 Clothiaux et al., 2000; Lim et al., 2019), the CBH retrievals from ceilometer or lidar
481 still bear some uncertainties, which can potentially lead to a mean bias of 0.1km (Silber
482 et al., 2018; Cromwell et a., 2019). In our method, a systematic increase of 0.1 km in
483 the CBH can lead to an increase of 2.1% in omission errors and a decrease of 1% in
484 commission errors.

485 After identifying the coupling state of clouds, it is feasible to retrieve the PBLH
486 under cloudy conditions. In particular, the DTDS-derived PBLH needs to resort to the
487 cloud position for coupled cloud cases. For decoupled cloud cases, on the other hand,
488 the PBLH blow clouds is sought to avoid cloud interference. For coupled clouds,
489 DTDS-derived PBLHs show a strong correlation with RS-derived PBLHs with a
490 correlation coefficient (R) of ~0.9 (Figure 10d). For decoupled cases, the correlation
491 between DTDS-derived PBLHs and RS-derived PBLHd is generally good (R = 0.73)
492 but worse than the correlation for coupled cases (Figure 10h). As pointed out in previous
493 studies (Chu et al., 2019; Hageli et al., 2000; Lewis et al., 2013; Su et al., 2017b), it has
494 been a persistent problem to retrieve the PBLH under cloudy conditions since the strong
495 backscattering and step signals from cloud interference would be excluded to avoid
496 interfering with the retrievals. The PBLH determined by our method under a cloudy
497 condition is much more reasonable. Moreover, due to the different definitions of the
498 PBLH and aerosol stratification within the PBL, there are always considerable

499 differences between lidar- and RS-derived PBLHs, which cannot be eliminated by a
500 specific algorithm (Chu et al., 2019; Su et al., 2020).

501

502 **5 Summary**

503 In this study, we proposed a novel method for distinguishing between coupled and
504 decoupled low clouds over land. Based on the understanding of PBL processes and
505 quantitative analyses, we developed a lidar-based method (DTDS) to identify the
506 coupling state of low clouds over the SGP site. In practice, we identified a coupled
507 cloud when the position of the cloud base was generally close to or lower than the
508 previous position of the PBL top, with the LCL serving as an additional restriction.
509 Compared to using the LCL alone, the coupled states identified by the DTDS method
510 show better consistency with the results derived from radiosondes, with about 10%
511 differences between the lidar-based retrievals and radiosonde results.

512 Not only coupled state, also retrieved by the method is the PBLH under cloudy
513 conditions. A long-lasting problem with lidar-retrieval of PBLH is either incapability
514 of retrieval or large uncertainties induced by the occurrence of low clouds (e.g., Chu et
515 al., 2019; Hageli et al., 2000; Lewis et al., 2013), we address this issue by separately
516 considering the coupled and decoupled of low clouds. Specifically, in coupled
517 conditions, the position of the coupled cloud serves as a good reference for identifying
518 the PBLH. In decoupled conditions, the large backscatter and step signals from clouds
519 would be excluded to avoid interfering with the retrievals. With our method, cloudy
520 conditions are well handled.

521 With the new method, we study the difference of cloud-PBL interactions in coupled
522 and decoupled conditions. In contrast to the sensitive responses of coupled clouds to
523 changes in the PBLH and buoyancy, the decoupled clouds and the PBLH are weakly
524 related. Due to their different relationships with the PBL, a robust distinguishment
525 between the coupled and decoupled low clouds is critical for further investigating the
526 coupled land-atmosphere system and aerosol-cloud interactions. Our methodology
527 paves a solid ground for such pursuits.

528

529 *Data availability.* All these datasets are publicly available at the ARM archive
530 https://adc.arm.gov/discovery/#/results/site_code::sgp. The products developed in this
531 study, i.e., cloud states and the PBLH, are currently available upon request from the
532 lead author (tianning@umd.edu) and are expected to be added to the ARM archive in
533 the near future.

534

535 *Author contribution.* T.S., Y.Z., and Z.L. conceptualized this study. T.S. carried out the
536 analysis, with comments from other co-authors. T.S., Y.Z., and Z.L. interpreted the data
537 and wrote the manuscript.

538

539 *Competing interests.* The authors declare that they have no conflict of interest.

540

541 *Acknowledgements.* This work was supported by grants from the U.S. Department of
542 Energy (DE-SC0018996), the National Science Foundation (AGS1837811), and NASA
543 (NNX16AN61G). We acknowledge the provision of radiosonde, MPL data, surface
544 meteorological data, and cloud products by the U.S. Department of Energy's ARM
545 program. We thank the two anonymous reviewers for their comments.

546

547 **References**

548 Berkes, F., Hoor, P., Bozem, H., Kunkel, D., Sprenger, M. and Henne, S. (2016).

549 Airborne observation of mixing across the entrainment zone during PARADE 2011.

550 *Atmospheric Chemistry and Physics*, 16(10), pp.6011-6025.

551 Betts, A.K. (2009). Land-surface-atmosphere coupling in observations and models.

552 *Journal of Advances in Modeling Earth Systems*, 1(3).

553 <https://doi.org/10.3894/JAMES.2009.1.4>

554 Bretherton, C. S., and Wyant, M. C. (1997). Moisture transport, lower-tropospheric

555 stability, and decoupling of cloud-topped boundary layers. *Journal of the*

556 *Atmospheric Sciences*, 54(1), 148–167. [https://doi.org/10.1175/1520-](https://doi.org/10.1175/1520-0469(1997)054<0148:MTL TSA>2.0.CO;2)

557 [0469\(1997\)054<0148:MTL TSA>2.0.CO;2](https://doi.org/10.1175/1520-0469(1997)054<0148:MTL TSA>2.0.CO;2)

558 Brooks, I. M. (2003). Finding boundary layer top: application of a wavelet covariance

559 transform to lidar backscatter profiles. *Journal of Atmospheric and Oceanic*

560 *Technology*, 20, 1092–1105. [https://doi.org/10.1175/1520-](https://doi.org/10.1175/1520-0426(2003)020<1092:FBLTAO>2.0.CO;2)

561 [0426\(2003\)020<1092:FBLTAO>2.0.CO;2](https://doi.org/10.1175/1520-0426(2003)020<1092:FBLTAO>2.0.CO;2)

562 Campbell, J. R., Hlavka, D. L., Welton, E. J., Flynn, C. J., Turner, D. D., Spinhirne, J.
563 D., ... Hwang, I. H. (2002). Full-time, eye-safe cloud and aerosol lidar
564 observation at atmospheric radiation measurement program sites: instruments and
565 data processing. *Journal of Atmospheric and Oceanic Technology*, 19(4), 431–442.
566 [https://doi.org/10.1175/1520-0426\(2002\)019<0431:FTESCA>2.0.CO;2](https://doi.org/10.1175/1520-0426(2002)019<0431:FTESCA>2.0.CO;2)

567 Campbell, J.R., Welton, E.J., Spinhirne, J.D., Ji, Q., Tsay, S.C., Piketh, S.J., Barenbrug,
568 M. and Holben, B.N., 2003. Micropulse lidar observations of tropospheric aerosols
569 over northeastern South Africa during the ARREX and SAFARI 2000 dry season
570 experiments. *Journal of Geophysical Research: Atmospheres*, 108(D13).

571 Cheruy, F., Dufresne, J. L., Hourdin, F., and Ducharne, A. (2014). Role of clouds and
572 land-atmosphere coupling in midlatitude continental summer warm biases and
573 climate change amplification in CMIP5 simulations. *Geophysical Research Letters*,
574 41(18), 6493–6500. <https://doi.org/10.1002/2014GL061145>

575 Chu, Y., Li, J., Li, C., Tan, W., Su, T., and Li, J. (2019). Seasonal and diurnal variability
576 of planetary boundary layer height in Beijing: intercomparison between MPL and
577 WRF results. *Atmospheric Research*, 227, 1–13.
578 <https://doi.org/10.1016/j.atmosres.2019.04.017>

579 Clothiaux, E. E., Ackerman, T. P., Mace, G. G., Moran, K. P., Marchand, R. T., Miller,
580 M. A., and Martner, B. E. (2000). Objective determination of cloud heights and
581 radar reflectivities using a combination of active remote sensors at the ARM CART
582 sites. *Journal of Applied Meteorology*, 39(5), 645–665.

583 [https://doi.org/10.1175/1520-0450\(2000\)039<0645:ODOCHA>2.0.CO;2](https://doi.org/10.1175/1520-0450(2000)039<0645:ODOCHA>2.0.CO;2)

584 Cromwell, E., and Flynn, D. (2019). Lidar cloud detection with fully convolutional
585 networks. In 2019 IEEE Winter Conference on Applications of Computer Vision
586 (WACV) (pp. 619-627). IEEE.

587 de Roode, S.R. and Wang, Q. (2007). Do stratocumulus clouds detrain? FIRE I data
588 revisited. *Boundary-layer meteorology*, 122(2), pp.479-491.

589 Demoz, B., Flamant, C., Weckwerth, T., Whiteman, D., Evans, K., Fabry, F., and
590 Schwemmer, G. (2006). The dryline on 22 May 2002 during IHOP_2002:
591 convective-scale measurements at the profiling site. *Monthly Weather Review*,
592 134(1), 294–310. <https://doi.org/10.1175/MWR3054.1>

593 Dong, X., Schwantes, A. C., Xi, B., and Wu, P. (2015). Investigation of the marine
594 boundary layer cloud and CCN properties under coupled and decoupled conditions
595 over the Azores. *Journal of Geophysical Research: Atmospheres*, 120, 6179–6191.
596 <https://doi.org/10.1002/2014JD022939>

597 Driedonks, A. G. M. (1982). Models and observations of the growth of the atmospheric
598 boundary layer. *Boundary-Layer Meteorology*, 23(3), 283–306.
599 <https://doi.org/10.1007/BF00121117>

600 Ek, M. B., and Holtslag, A. A. M. (2004). Influence of soil moisture on boundary layer
601 cloud development. *Journal of Hydrometeorology*, 5(1), 86–99.
602 [https://doi.org/10.1175/1525-7541\(2004\)005<0086:IOSMOB>2.0.CO;2](https://doi.org/10.1175/1525-7541(2004)005<0086:IOSMOB>2.0.CO;2)

603 Flynn, D., Shi, Y., Lim, K., and Riihimaki, L. (2017). Cloud Type Classification
604 (cldtype) Value-Added Product. Ed. by Robert Stafford, ARM Research Facility.
605 DOE/SC-ARM-TR-200.

606 Garratt, J. R. (1994). Review: the atmospheric boundary layer. *Earth-Science Reviews*,
607 37(1-2), 89–134. [https://doi.org/10.1016/0012-8252\(94\)90026-4](https://doi.org/10.1016/0012-8252(94)90026-4)

608 Glenn, I. B., Feingold, G., Gristey, J. J., and Yamaguchi, T. (2020). Quantification of
609 the radiative effect of aerosol-cloud-interactions in shallow continental cumulus
610 clouds. *Journal of the Atmospheric Sciences*, 77, 2905–2920.
611 <https://doi.org/10.1175/JAS-D-19-0269.1>

612 Golaz, J. C., Larson, V. E., and Cotton, W. R. (2002). A PDF-based model for boundary
613 layer clouds. Part I: Method and model description. *Journal of the Atmospheric*
614 *Sciences*, 59(24), 3540–3551. [https://doi.org/10.1175/1520-](https://doi.org/10.1175/1520-0469(2002)059<3540:APBMFB>2.0.CO;2)
615 [0469\(2002\)059<3540:APBMFB>2.0.CO;2](https://doi.org/10.1175/1520-0469(2002)059<3540:APBMFB>2.0.CO;2)

616 Guo, J., Miao, Y., Zhang, Y., Liu, H., Li, Z., Zhang, W., ... Zhai, P. (2016). The
617 climatology of planetary boundary layer height in China derived from radiosonde
618 and reanalysis data. *Atmospheric Chemistry and Physics*, 16(20), 13,309–13,319.
619 <https://doi.org/10.5194/acp-16-13309-2016>

620 Hageli, P., Steyn, D. G., and Strawbridge, K. B. (2000). Spatial and temporal variability
621 of mixed-layer depth and entrainment zone thickness. *Boundary-Layer*
622 *Meteorology*, 97, 47–71. <https://doi.org/10.1023/A:1002790424133>

623 Holdridge, D., Ritsche, M., Prell, J., and Coulter, R. (2011). Balloon-borne sounding

624 system (SONDE) handbook. <https://www.arm.gov/capabilities/instruments/sonde>

625 Holzworth, G. C., (1964). Estimates of mean maximum mixing depths in the contiguous
626 United States, *Mon. Weather Rev.*, 92, 235–242, [https://doi.org/10.1175/1520-](https://doi.org/10.1175/1520-0493(1964)092<0235:eommmmd>2.3.co;2)
627 0493(1964)092<0235:eommmmd>2.3.co;2.

628 Jones, C., Bretherton, C., and Leon, D. (2011). Coupled vs. decoupled boundary layers
629 in VOCALS-REx. *Atmospheric Chemistry and Physics*, 11(14), 7143–7153.
630 <https://doi.org/10.5194/acp-11-7143-2011>

631 Kasahara, A. (1974). Various vertical coordinate systems used for numerical weather
632 prediction. *Monthly Weather Review*, 102(7), 509–522.
633 [https://doi.org/10.1175/1520-0493\(1974\)102<0509:VVCSUF>2.0.CO;2](https://doi.org/10.1175/1520-0493(1974)102<0509:VVCSUF>2.0.CO;2)

634 Lewis, J. R., Welton, E. J., Molod, A. M., and Joseph, E. (2013). Improved boundary
635 layer depth retrievals from MPLNET. *Journal of Geophysical Research: Atmospheres*, 118(17), 9870–9879. <https://doi.org/10.1002/jgrd.50570>

637 Lim, K.S.S., Riihimaki, L.D., Shi, Y., Flynn, D., Kleiss, J.M., Berg, L.K., Gustafson,
638 W.I., Zhang, Y. and Johnson, K.L. (2019). Long-term retrievals of cloud type and
639 fair-weather shallow cumulus events at the ARM SGP site. *Journal of Atmospheric and Oceanic Technology*, 36(10), pp.2031-2043.

641 Liu, S. Y., and Liang, X. Z. (2010). Observed diurnal cycle climatology of planetary
642 boundary layer height. *Journal of Climate*, 23, 5790–5809.
643 <https://doi.org/10.1175/2010JCLI3552.1>

644 Lock, A. P., Brown, A. R., Bush, M. R., Martin, G. M., & Smith, R. N. B. (2000). A
645 new boundary layer mixing scheme. Part I: Scheme description and single-column
646 model tests. *Monthly weather review*, 128(9), 3187-3199.

647 Nicholls, S. (1984). The dynamics of stratocumulus: aircraft observations and
648 comparisons with a mixed layer model. *Quarterly Journal of the Royal*
649 *Meteorological Society*, 110(466), 783–820.
650 <https://doi.org/10.1002/qj.49711046603>

651 Ott, L. E., Bacmeister, J., Pawson, S., Pickering, K., Stenchikov, G., Suarez, M., ... and
652 Xueref-Remy, I. (2009). Analysis of convective transport and parameter sensitivity
653 in a single column version of the Goddard earth observation system, version 5,
654 general circulation model. *Journal of the Atmospheric Sciences*, 66(3), 627-646.

655 Platt, C. M., Young, S. A., Carswell, A. I., Pal, S. R., McCormick, M. P., Winker, D.
656 M., ... and Wooldridge, C. (1994). The Experimental Cloud Lidar Pilot Study
657 (ECLIPS) for cloud-radiation research. *Bulletin of the American Meteorological*
658 *Society*, 75, 1635–1654. [https://doi.org/10.1175/1520-](https://doi.org/10.1175/1520-0477(1994)075<1635:TECLPS>2.0.CO;2)
659 [0477\(1994\)075<1635:TECLPS>2.0.CO;2](https://doi.org/10.1175/1520-0477(1994)075<1635:TECLPS>2.0.CO;2)

660 Revercomb, H.E., Turner, D.D., Tobin, D.C., Knuteson, R.O., Feltz, W.F., Barnard, J.,
661 Bösenberg, J., Clough, S., Cook, D., Ferrare, R. and Goldsmith, J., 2003. The ARM
662 program's water vapor intensive observation periods: Overview, initial
663 accomplishments, and future challenges. *Bulletin of the American Meteorological*
664 *Society*, 84(2), pp.217-236.

665 Romps, D. M. (2017). Exact expression for the lifting condensation level. *Journal of*
666 *the Atmospheric Sciences*, 74(12), 3891–3900. [https://doi.org/10.1175/JAS-D-17-](https://doi.org/10.1175/JAS-D-17-0102.1)
667 [0102.1](https://doi.org/10.1175/JAS-D-17-0102.1)

668 Santanello Jr., J. A., Dirmeyer, P. A., Ferguson, C. R., Findell, K. L., Tawfik, A. B.,
669 Berg, A., ... and Roundy, J. (2018). Land–atmosphere interactions: the LoCo
670 perspective. *Bulletin of the American Meteorological Society*, 99(6), 1253–1272.
671 <https://doi.org/10.1175/BAMS-D-17-0001.1>

672 Sawyer, V., and Li, Z. Q. (2013). Detection, variations and intercomparison of the
673 planetary boundary layer depth from radiosonde, lidar and infrared spectrometer.
674 *Atmospheric Environment*, 79, 518–528.
675 <https://doi.org/10.1016/j.atmosenv.2013.07.019>

676 Seidel, D. J., Ao, C. O., and Li, K. (2010). Estimating climatological planetary boundary layer
677 heights from radiosonde observations: Comparison of methods and uncertainty analysis.
678 *Journal of Geophysical Research: Atmospheres*, 115(D16).

679 Silber, I., J. Verlinde, E. W. Eloranta, C. J. Flynn, and D. M. Flynn (2018), Polar liquid
680 cloud base detection algorithms for high spectral resolution or micropulse lidar data,
681 *J. Geophys. Res.: Atmos.*, doi: 10.1029/2017JD027840.

682 Storer, R.L., Griffin, B.M., Höft, J., Weber, J.K., Raut, E., Larson, V.E., Wang, M. and
683 Rasch, P.J. (2015). Parameterizing deep convection using the assumed probability
684 density function method. *Geoscientific Model Development*, 8(1), pp.1-19.

685 Stull, R. B. (1988). *An Introduction to Boundary Layer Meteorology*. Dordrecht:

686 Springer Netherlands.

687 Su, T., Li, J., Li, C. C., Xiang, P. Z., Lau, A. K. H., Guo, J. P., ... and Miao, Y. C. (2017b).

688 An intercomparison of long-term planetary boundary layer heights retrieved from

689 CALIPSO, ground-based lidar, and radiosonde measurements over Hong Kong.

690 *Journal of Geophysical Research: Atmospheres*, 122, 3929–3943.

691 <https://doi.org/10.1002/2016JD025937>

692 Su, T., Li, J., Li, J., Li, C., Chu, Y., Zhao, Y., ... Wang, L. (2017a). The evolution of

693 springtime water vapor over Beijing observed by a high dynamic Raman lidar

694 system: case studies. *IEEE Journal of Selected Topics in Applied Earth*

695 *Observations and Remote Sensing*, 10(5), 1715–1726.

696 <https://doi.org/10.1109/JSTARS.2017.2653811>

697 Su, T., Li, Z., and Kahn, R. (2018). Relationships between the planetary boundary layer

698 height and surface pollutants derived from lidar observations over China: regional

699 pattern and influencing factors. *Atmospheric Chemistry and Physics*, 18(21),

700 15,921–15,935. <https://doi.org/10.5194/acp-18-15921-2018>

701 Su, T., Li, Z., and Kahn, R. (2020). A new method to retrieve the diurnal variability of

702 planetary boundary layer height from lidar under different thermodynamic stability

703 conditions. *Remote Sensing of Environment*, 237, 111519.

704 <https://doi.org/10.1016/j.rse.2019.111519>

705 Teixeira, J., and Hogan, T. F. (2002). Boundary layer clouds in a global atmospheric

706 model: simple cloud cover parameterizations. *Journal of Climate*, 15(11), 1261–

707 1276. <https://doi.org/10.1175/1520->
708 0442(2002)015<1261:BLCIAG>2.0.CO;Vogelezang, D. H. P., and Holtslag, A. A.
709 M. (1996). Evaluation and model impacts of alternative boundary-layer height
710 formulations. *Boundary-Layer Meteorology*, 81(3-4), 245–269.
711 <https://doi.org/10.1007/BF02430331>

712 Wallace, J. M., and Hobbs, P. V. (2006). *Atmospheric Science: an Introductory Survey*.
713 Amsterdam, Boston: Elsevier Academic Press.

714 Warren, G., Hahn, C. J., London, J., Chervin, M., and Jenne, R. L. (1986). Global
715 distribution of total cloud cover and cloud type amounts over land. (Rep. DOE/ER-
716 0406). Washington, DC: U.S. DOE Office of Energy Research.

717 Wei, J., Huang, W., Li, Z., Sun, L., Zhu, X., Yuan, Q., Liu, L. and Cribb, M., 2020.
718 Cloud detection for Landsat imagery by combining the random forest and
719 superpixels extracted via energy-driven sampling segmentation approaches.
720 *Remote Sensing of Environment*, 248, p.112005.

721 Welton, E. J., Campbell, J. R., Spinhirne, J. D., and Scott III, V. S. (2001). Global
722 monitoring of clouds and aerosols using a network of micropulse lidar systems. In
723 *Lidar Remote Sensing for Industry and Environment Monitoring* (Vol. 4153, 151–
724 158). International Society for Optics and Photonics.

725 Wu, X., Grabowski, W. W, and Moncrieff, M. W. (1998). Long-term behavior of cloud
726 systems in TOGA COARE and their interactions with radiative and surface
727 processes. Part I: Two-dimensional modeling study. *Journal of the Atmospheric*

728 *Sciences*, 55(17), 2693–2714. <https://doi.org/10.1175/1520->
729 [0469\(1998\)055<2693:LTBOCS>2.0.CO;2](https://doi.org/10.1175/1520-0469(1998)055<2693:LTBOCS>2.0.CO;2)

730 Yang, D., Li, C., Lau, A. K. H., and Li, Y. (2013). Long-term measurement of daytime
731 atmospheric mixing layer height over Hong Kong. *Journal of Geophysical*
732 *Research: Atmospheres*, 118(5), 2422–2433. <https://doi.org/10.1002/jgrd.50251>

733 Yang, T., Wang, Z., Zhang, W., Gbaguidi, A., Sugimoto, N., Wang, X., Matsui, I. and
734 Sun, Y., 2017. Boundary layer height determination from lidar for improving air
735 pollution episode modeling: development of new algorithm and evaluation.
736 *Atmospheric Chemistry and Physics*, 17(10), p.6215.

737 Zhao, C., Wang, Y., Wang, Q., Li, Z., Wang, Z., and Liu, D. (2014). A new cloud and
738 aerosol layer detection method based on micropulse lidar measurements. *Journal*
739 *of Geophysical Research: Atmospheres*, 119(11), 6788–6802.
740 <https://doi.org/10.1002/2014JD021760>

741 Zheng, Y., and Li, Z. (2019). Episodes of warm-air advection causing cloud-surface
742 decoupling during the MARCUS. *Journal of Geophysical Research: Atmospheres*,
743 124(22). <https://doi.org/10.1029/2019JD030835>

744 Zheng, Y., and Rosenfeld, D. (2015). Linear relation between convective cloud base
745 height and updrafts and application to satellite retrievals. *Geophysical Research*
746 *Letters*, 42(15), 6485–6491. <https://doi.org/10.1002/2015GL064809>

747 Zheng, Y., Rosenfeld, D., and Li, Z. (2018). Estimating the decoupling degree of
748 subtropical marine stratocumulus decks from satellite. *Geophysical Research*

749 *Letters*, 45. <https://doi.org/10.1029/2018GL078382>

750 Zheng, Y., Sakradzija, M., Lee, S.-S., and Li, Z. (2020). Theoretical understanding of
751 the linear relationship between convective updrafts and cloud-base height for
752 shallow cumulus clouds. Part II: Continental conditions. *Journal of the*
753 *Atmospheric Sciences*, 77, 1313–1328. <https://doi.org/10.1175/JAS-D-19-0301.1>

754

755 Tables

756 **Table 1. List of parameters in the flow chart of DTDS (Figure 4). These parameters**
757 **are related with three factors, including LCL, PBLH, CBH. The sensitivity of**
758 **selection of these parameters is presented. The detailed impacts of variations in**
759 **these parameters on the retrievals of cloud coupling and PBLH are presented in**
760 **Figure 6 and Figure 7, respectively.**

761

	Unit	Related factors	Value	Sensitivity (coupled states)	Sensitivity (PBLH)
A_1	km	LCL / PBLH	0.7	Low	Low ⁷⁶⁴
A_2	km	PBLH	0.2	High	Low ⁷⁶⁵
A_3	km	LCL	0.15	Low	Low ⁷⁶⁶
A_4	dimensionless	CBH	1.35	Low	Low ⁷⁶⁷
A_5	dimensionless	CBH	1.1	Low	High ⁷⁶⁸

769

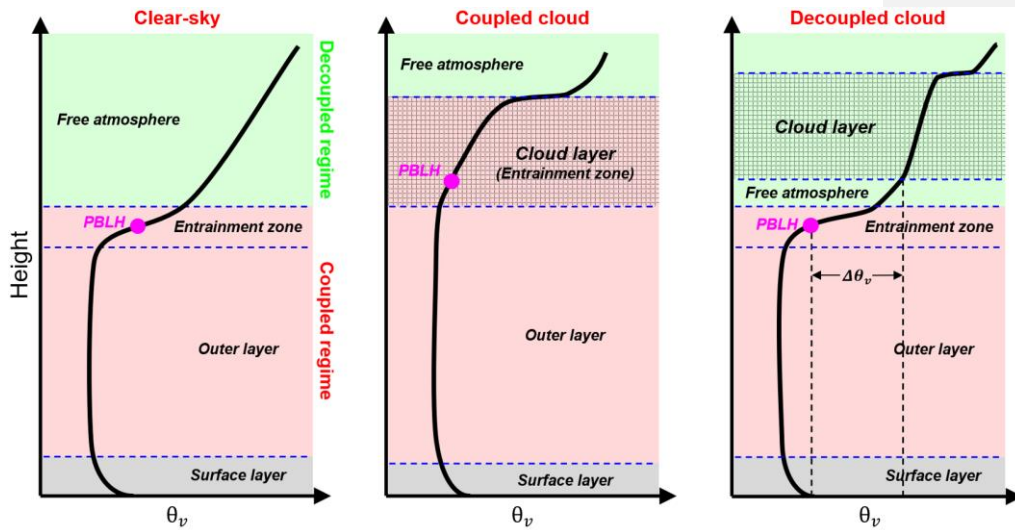
770

771

Formatted: Font: Bold

Formatted: Font: Bold

772 **Figures**

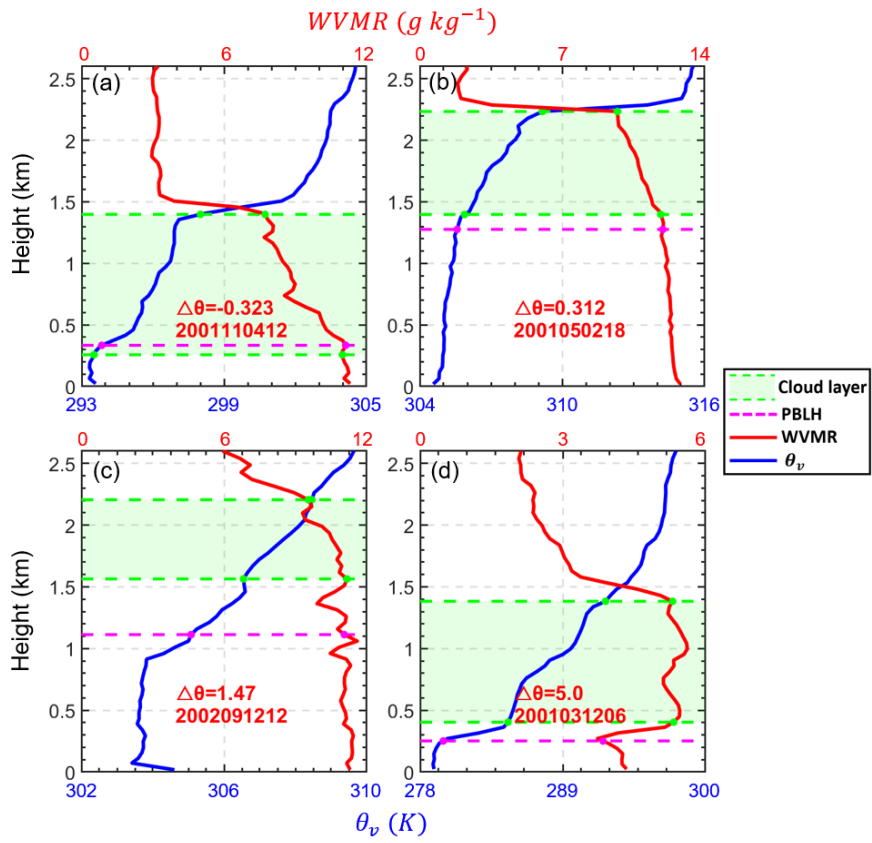


773

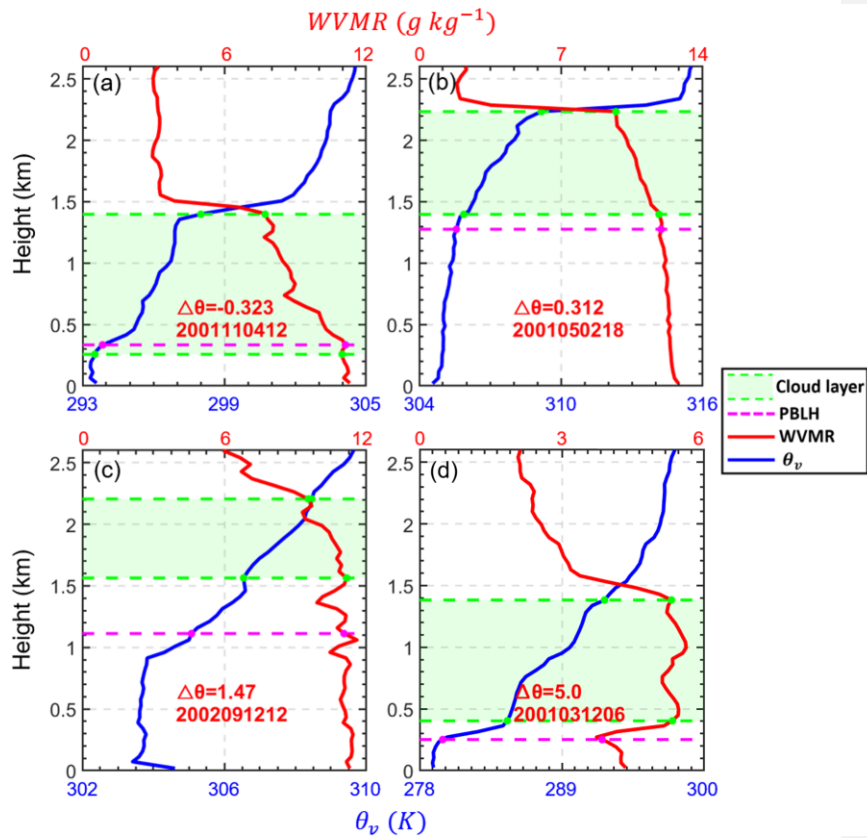
774 **Figure 1.** Idealized vertical profiles of virtual potential temperature (θ_v) under the clear-
 775 sky, coupled cloud, and decoupled cloud over land. The surface layer, outer layer
 776 entrainment zone, and free atmosphere are divided by the blue dash lines. The cloudy
 777 layer is marked as the shaded area, and PBLH is marked as the pink point. Red and
 778 green zones indicate the coupled and decoupled regime, respectively. Elements (e.g.,
 779 turbulence, heat fluxes, cloud) in the coupled regime are directly affected by the PBL
 780 processes, while these elements are not directly affected by the PBL processes in the
 781 decoupled regime. For the coupled cases, the cloud base is below the capping inversion
 782 of entrainment zone. For the decoupled cases, the cloud base is above the capping
 783 inversion.

784

785



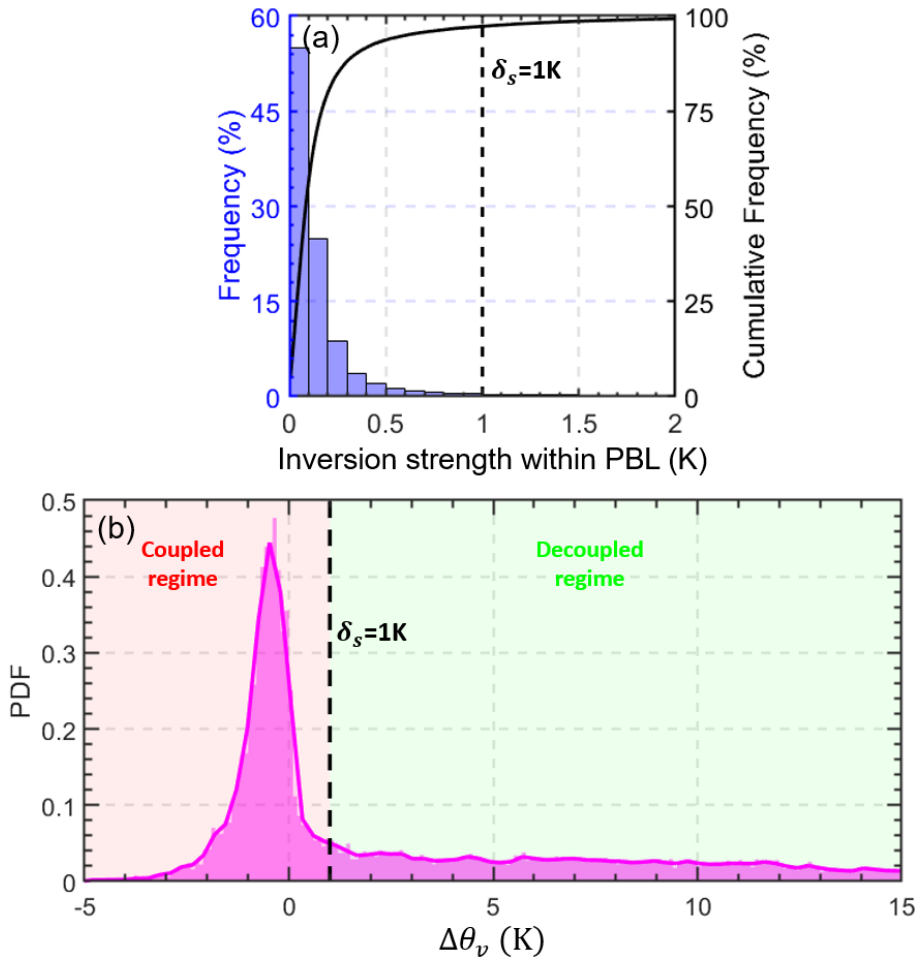
786



787

788 **Figure 2.** Virtual potential temperature (θ_v , ~~blue~~ ~~red~~ lines) and water vapor mixing ratio
 789 (WVMR, ~~red~~ ~~blue~~ lines) profiles from radiosonde (RS) over the Southern Great Plains
 790 site for different cases. The differences in virtual potential temperature between the
 791 cloud base and the planetary boundary layer (PBL) top are expressed as $\Delta\theta_v$ ($\theta_v^{\text{CBH}} -$
 792 θ_v^{PBLH}). The time of each radiosonde launch is marked in each panel as
 793 “YYYYMMDDHH”, where YYYY, MM, DD, and HH indicates the year, month, day,
 794 and local time, respectively. Green regions are cloud layers, and green dashed lines
 795 indicate their boundaries. The cloud layer is obtained from the CLDTYPE/ARSCL data.

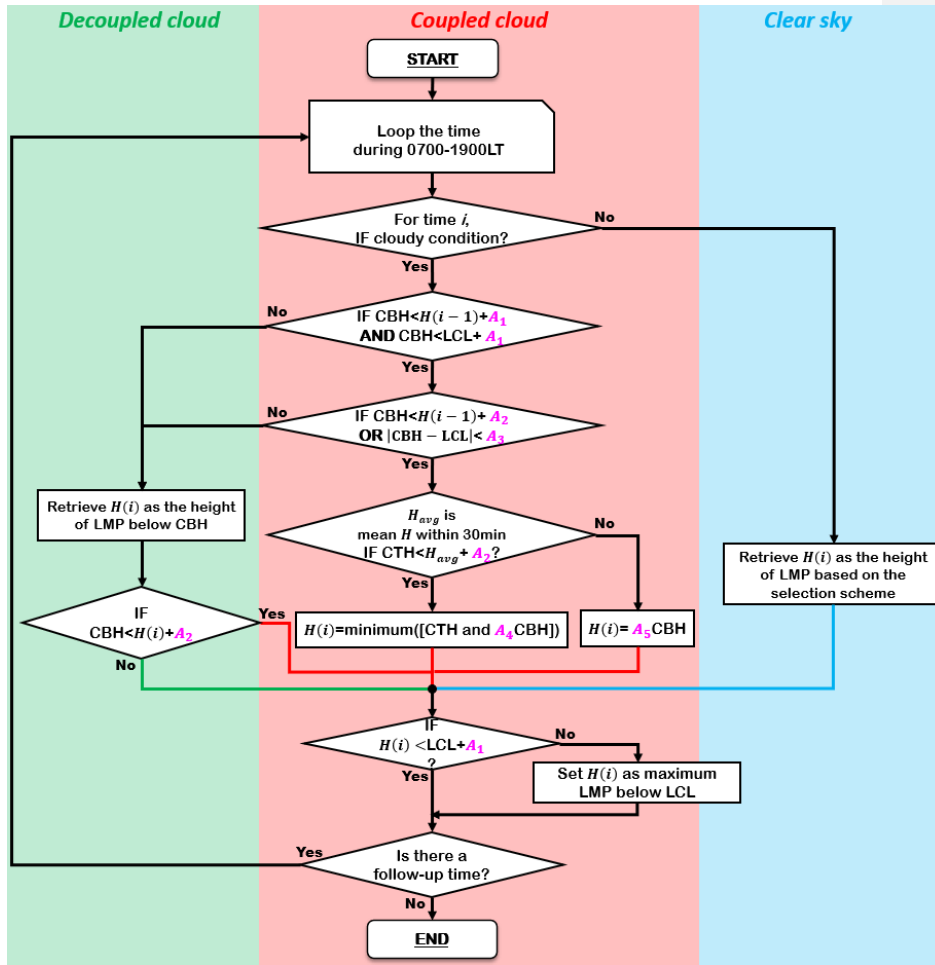
796 PBLHs is derived from RS data, and is marked as dashed pink lines.



797

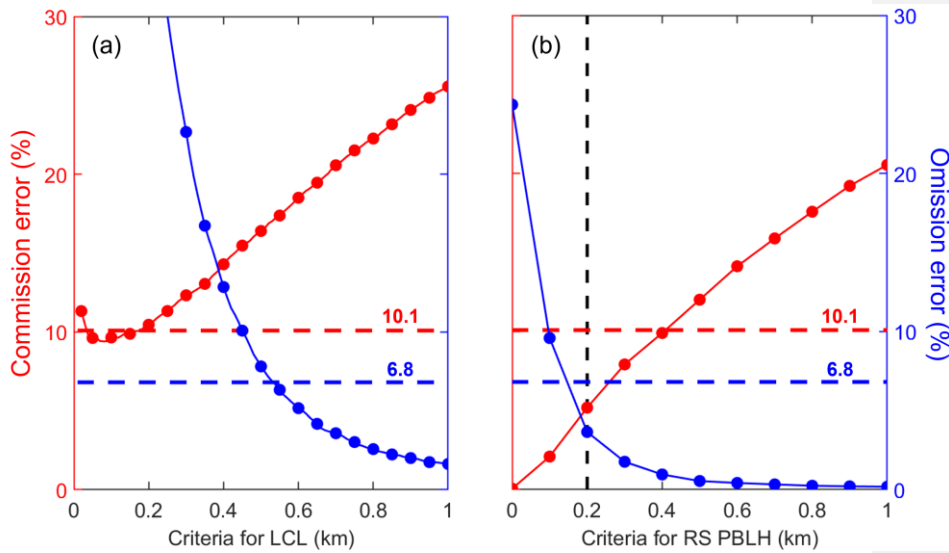
798 **Figure 3.** (a) Blue bars represent the inversion strength of θ_v within the PBL. The
 799 inversion strength is derived from the radiosonde during daytime (0800-1900LT). The
 800 inversions near surface or across PBL top are excluded. The black solid line represents
 801 cumulative frequency. (b) Pink area represents the probability density function (PDF)
 802 of the differences in the virtual potential temperature between cloud-base height (CBH)
 803 and PBLH ($\Delta\theta_v = \theta_v^{\text{CBH}} - \theta_v^{\text{PBLH}}$). By using a threshold of $\Delta\theta_v < \delta_s$ (1 K), we can

804 identify the coupled cloud regime. By using a threshold of δ_s (1-K), coupled and
 805 decoupled regimes are classified.



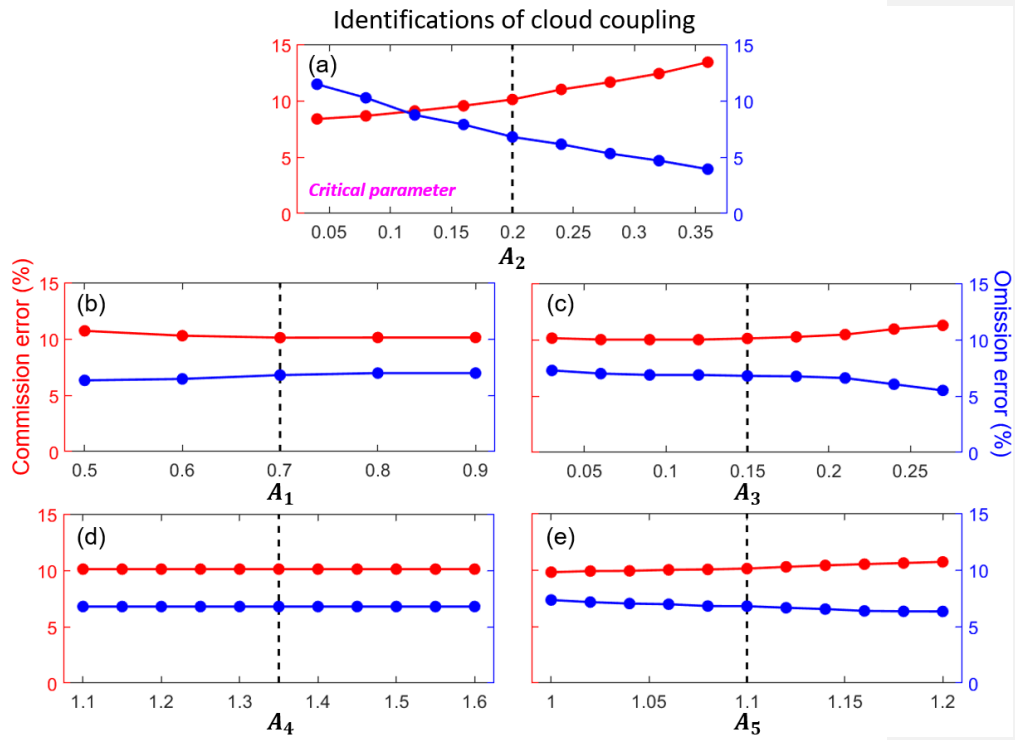
806
 807 **Figure 4.** The flow chart of the updated DTDS algorithm. In this diagram, $H(i)$ is the
 808 retrieved planetary boundary layer height (PBLH) at time i . CBH and CTH represent
 809 the base and top heights, respectively, of the lowest cloud at time i . The PBLH part for
 810 selecting the suitable local maximum position (LMP) follows Su et al. (2020), and a
 811 detailed scheme for identifying a coupled cloud is added to the DTDS algorithm. LCL

812 stands for lifted condensation level. Five empirical parameters (A_1, A_2, A_3, A_4, A_5) are
 813 set as 0.7, 0.2, 0.15, 1.35, 1.1, respectively.



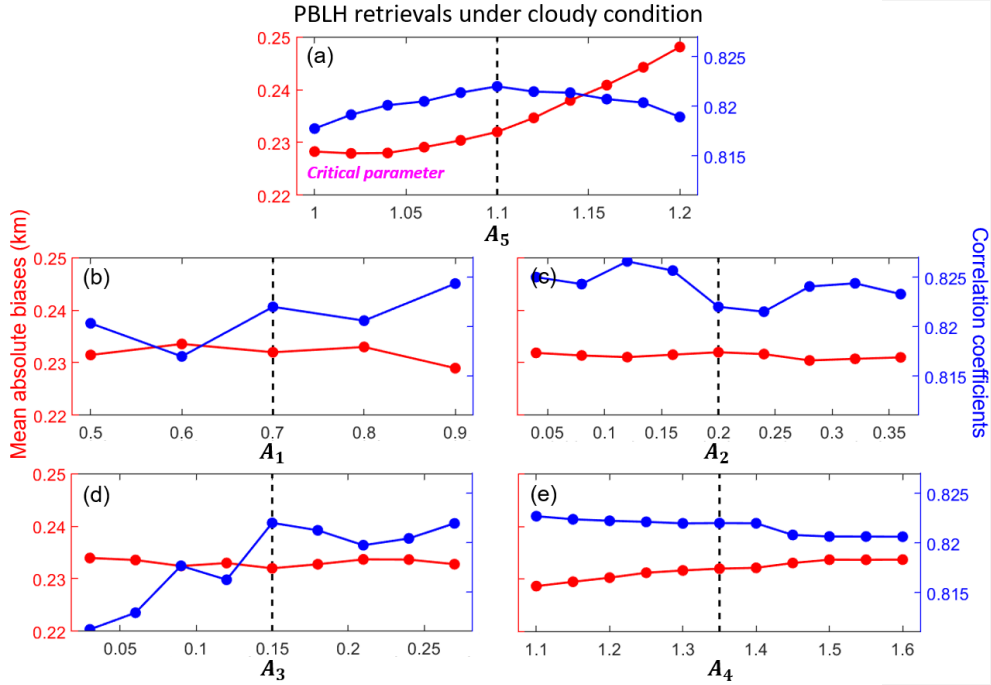
814
 815 **Figure 5.** Commission errors and omission errors of coupled cloud identifications (a)
 816 for different criteria for the lifted condensation level (LCL) and (b) for different criteria
 817 for the planetary boundary layer height (PBLH). “Criteria for LCL” means coupled
 818 clouds are identified if $|CBH - LCL| < \text{Criteria for LCL}$. Similarly, “Criteria for RS
 819 PBLH” means coupled clouds are identified if $CBH - RS\ PBLH < \text{Criteria for RS}$
 820 PBLH. The red and blue dashed lines indicate the commission and omission errors,
 821 respectively, for the DTDS algorithm. CBH stands for cloud-base height, and RS stands
 822 for radiosonde. By using ~ 7500 RS profiles, the cloud coupling state derived from the
 823 virtual potential temperature method (Section 3.1) is considered as the ground truth for
 824 evaluation.

825



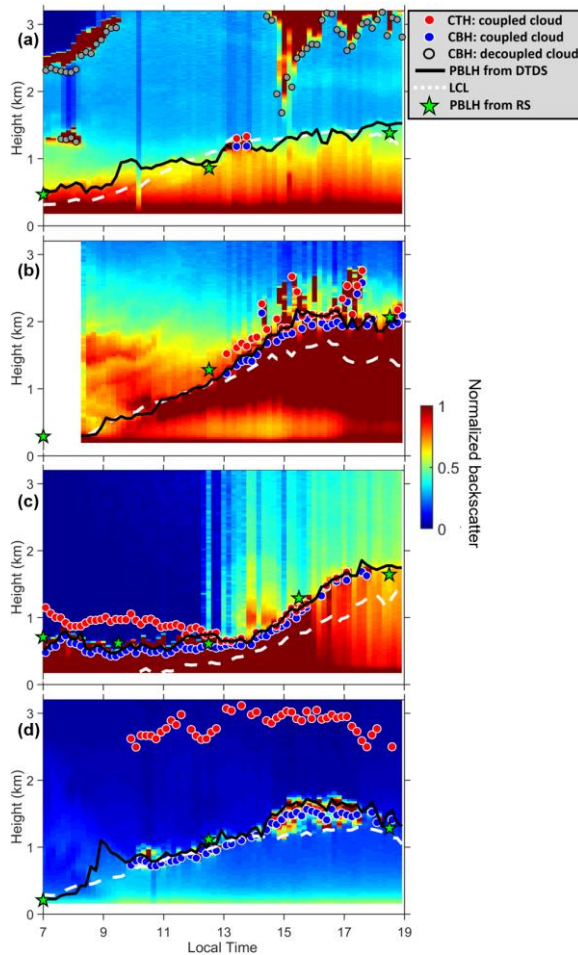
827

828 **Figure 6.** Commission errors (red line) and omission errors (blue line) of coupled cloud
 829 identifications for selecting different values of empirical parameters (A_1, A_2, A_3, A_4, A_5)
 830 in the DTDS algorithm. Black dash lines indicate the default values. For each test, one
 831 parameter is variable, while other parameters are set as default values. For
 832 identifications of cloud coupling, A_2 is the critical parameter.



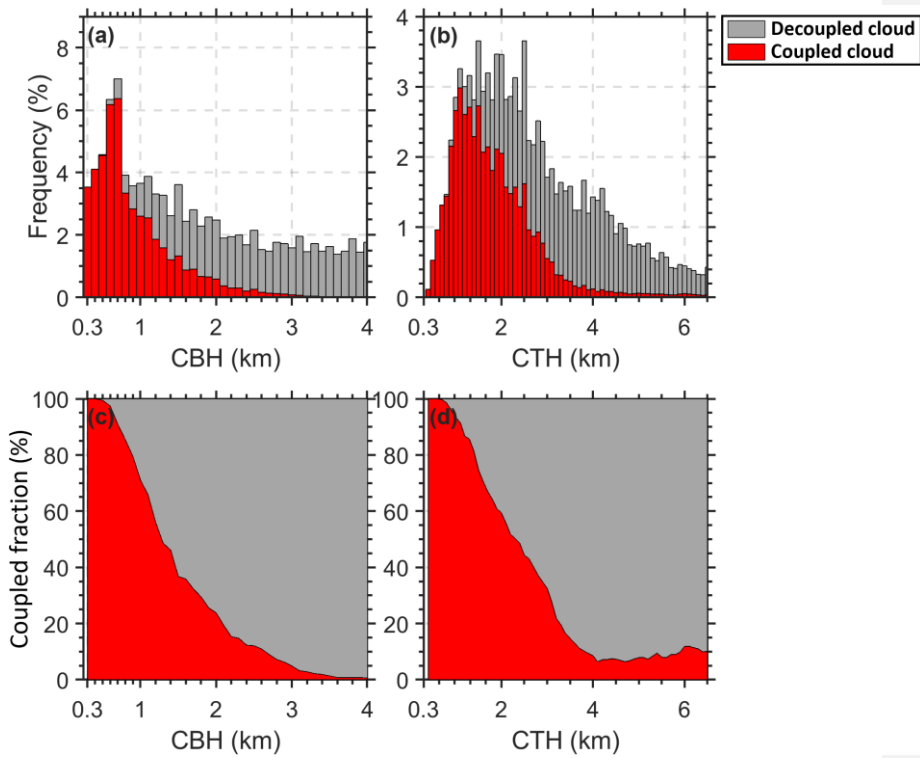
833

834 **Figure 7.** Red lines indicate the mean absolute biases between PBLH derived from lidar
 835 and radiosonde for selecting different values of empirical parameters (A_1, A_2, A_3, A_4, A_5)
 836 in the DTDS algorithm. Here, we only analyze the low cloud cases. Blue lines indicate
 837 the corresponding correlation coefficients between PBLH derived from lidar and
 838 radiosonde. Black dash lines indicate the default values. For each test, one parameter is
 839 variable, while other parameters are set as default values. For PBLH retrievals under
 840 cloudy conditions, A_5 is the critical parameter.



841

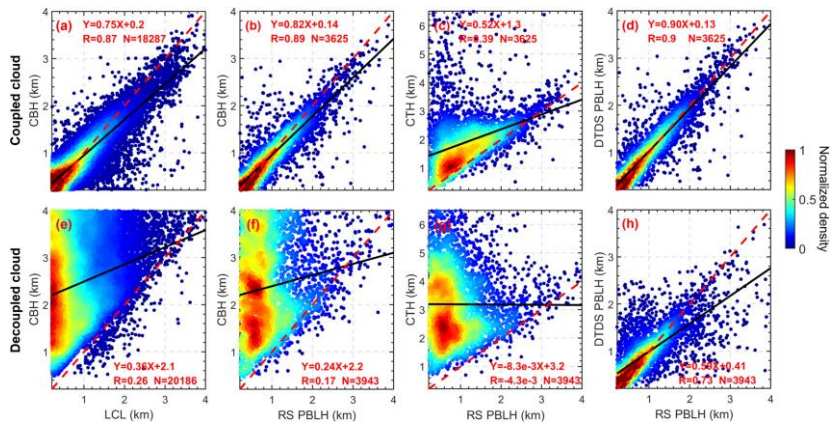
842 **Figure 8.** Daily backscatter profiles: (a) short-lived coupled cloud, (b) developed
 843 coupled cloud, (c) daylong coupled cloud, and (d) active coupled cloud. Backscatter is
 844 normalized to a range of 0–1 in arbitrary units. Red dots and blue dots indicate cloud-
 845 top heights (CTHs) and cloud-base heights (CBHs) of coupled clouds. Grey dots mark
 846 CBHs for decoupled clouds. Black lines and green stars mark the planetary boundary
 847 layer height (PBLH) retrieved from the DTDS algorithm and from radiosonde (RS)
 848 soundings, respectively. White dashed lines represent lifted condensation levels (LCLs).



849

850 **Figure 9.** The height-dependent occurrence frequencies of (a) the cloud-base height
 851 (CBH) and (b) the cloud-top height (CTH) for coupled clouds (red bars) and decoupled
 852 clouds (grey bars). The relative occurrence frequencies of (c) the CBH and (d) the CTH
 853 for coupled clouds (red area) and decoupled clouds (grey area).

854



855

856 **Figure 10.** The relationships between (a) LCL and CBH, (b) CBH and RS-derived
 857 PBLH, (c) CTH and RS-derived PBLH for coupled clouds, and (d) DTDS-derived
 858 PBLH and RS-derived PBLH. Panels (e-h) are similar to panels (a-d) but for decoupled
 859 clouds. Black lines represent the linear regressions. The linear fitting functions,
 860 correlation coefficients (R), and sampling numbers (N) are given in each panel.